Needle-like Ferroelastic Domains in Individual Ferroelectric Nanoparticles

*Zhen Liu, Elijah Schold, Dmitry Karpov, Ross Harder, Turab Lookman, and Edwin Fohtung**

Dr. Z. Liu, Dr. T. Lookman, Prof. E. Fohtung
Los Alamos National Laboratory, Los Alamos, NM 87545, USA
E-mail: fohtue@rpi.edu

E. Schold, Prof. E. Fohtung
Department of Materials Science and Engineering, Rensselaer Polytechnic Institute, 110 8th St, Troy, NY, 12180, USA

Dr. D. Karpov
Paul Scherrer Institute, Swiss Light Source, 5232 PSI-Villigen, Switzerland

Dr. R. Harder
Advanced Photon Source, Argonne National Laboratory, 9700 S Cass Ave, Lemont, IL, 60439, USA

Keywords: ferroelastic domains, domain boundaries, barium titanate, diffractive imaging, axial stress

Superior structural, physical and electronic properties make ferroelectric nanocrystals essential in enabling a range of next-generation devices. Ferroelectric responses are determined by crystal structure and domain morphology. The ability to reversibly displace, create and annihilate elastic domains is critical to device applications. Whereas electric-field control has been demonstrated for ferroelectric 180° surface domain walls and vortices, similar control of ferroelastic domains and domain boundaries within individual nanocrystals remains challenging. Using controlled external compressive and tensile axial stress, deterministic and reversible control of highly mobile ferroelastic domains and axial polarization in three dimensions is demonstrated. While many studies exist on ferroelastic domains in thin films and bulk, little is known about ferroelastic interactions at the single nanoparticle level, especially involving domain boundaries. Through combining Bragg coherent X-ray diffractive imaging and Landau theory, strain gradients in individual $BaTiO_3$ nanocrystals are shown to stabilize needle-like ferroelastic twin domains. These domains are highly labile under applied axial stress, producing a locally enhanced electric polarization

mediated by a ferroelectric phase transition. The efficacy of Bragg coherent X-ray diffractive imaging in studying in operando domains in three-dimensions is demonstrated, while synergy with theory provides a paradigm for domain boundary engineering and potential for nanoscale functional devices.

1. Introduction

Ferroelectric materials such as barium titanate ($BaTiO_3$, BTO) offer many functional properties that make them attractive in a wide variety of fields, with applications including radio-frequency filters in telecommunications and medical imaging systems,[1,2] sensing applications,[3] and non-volatile ferroelectric-based memories for low-power devices.[4] Most properties of ferroelectrics are influenced by the configuration of ferroelectric polarization,[5] and ferroelastic domain structure and switching dynamics.[3,4,6–13] For a review on the role of ferroelasticity in multiferroics, see Ref. [14]. To minimize the elastic energy,[15] bulk ferroelectrics break up into elastic domains, whose size distribution and relative orientation are of key importance for device applications. Furthermore, emergent functionalities,[16,17] emanating from domain walls — such as their ability to host itinerant electrons — make them potential hosts for charge conductivity,[18–21] as well as superconductivity, as measured in twinned crystals of WO_3,[22] and have made ferroelastic domains and domain boundaries interesting objects of study for their fundamental and applied science.[23–25]

In certain ferroelectrics such as BTO thin films, elastic domains typically consist of periodic parallel stripes of alternating crystallographic orientations known as polytwins (alternating a and c crystallographic orientations) accompanied by in-plane and out-of-plane polarizations, respectively.[26,27] Two-dimensional ferroelectric and ferroelastic domains have been extensively studied experimentally,[28,29] using surface scanning probes such as: high-resolution transmission electron microscopy,[30,31] atomic force microscopy,[26] and numerous optical based experimental techniques.[32] However, the three-dimensional evolution of elastic domains and their boundaries, the axial ferroelectric polarization, and the interplay and evolution of these structure-property relationships under the influence of external perturbations (such as external electric field and axial stress) remain elusive. Due to the fundamental limitations of two-dimensional surface scanning probes to access volumetric information at the nanoscale, the ability to noninvasively probe the volume of individual nanocrystals *in situ* and *operando* remains an ongoing challenge.

2. Results and Discussion

Here we use X-ray Bragg Coherent Diffractive Imaging (BCDI)[5,33,34] in conjunction with Landau theory to spatially resolve the three-dimensional (3D) structure of ferroelastic twins in individual BTO nanocrystals with nanoscale resolution. Ferroelectric phase transitions, as well as the behavior and evolution of elastic domains and axial ferroelectric polarization are studied under the influence of external tensile and compressive stress. The penetrating ability of coherent X-ray probes, the sensitivity of BCDI to local elastic strain, and the combination

of BCDI with theoretical Landau calculations provides us with a unique ability to probe and predict the volumetric behavior of structure-property relationships in individual BTO ferroelectric nanocrystals at the nanoscale.

The experimental setup and schematic for our Bragg coherent X-ray diffraction experiment is shown in **Figure 1**. Scanning electron microscopy is utilized to observe that the individual BTO nanocrystals have well defined facets with approximate diameters of 100-500 nm. Room temperature BTO is typically in the stable tetragonal phase with space group P4/mmm.[35] We used X-ray powder diffraction to confirm the crystalline nature of the BTO nanopowder sample as being in this tetragonal phase consistent with ICSD card 29148. Using an incident focused coherent X-ray beam of 9 KeV, we performed a rocking curve to collect 3D Bragg coherent diffraction data in the vicinity of the BTO (110) reciprocal lattice point. Figure 1 shows a slice of the 3D Bragg peak. The observed asymmetrical nature of our measured Bragg peak in Figure 1 is a characteristic signature of elastic strain and twinning of the ferroelectric crystals.[36,37] It is worth noting that a diffuse cloud about a measured X-ray Bragg peak in ferroelastic materials has been attributed to tweed (e.g. in the high T_c - superconductor $YBaCu_3O_{7-\delta}$).[38] Polar tweed at and above room temperature has also been observed in BTO at the surface (e.g. using photoemission electron microscopy),[39] and in the bulk (e.g. using resonant piezoelectric spectroscopy).[40] The observed diffuse cloud about our measured Bragg peak and the room temperature condition of our study mean that we cannot rule out the possibility of a tweed structural pattern in our sample. For inhomogenously strained crystals, expected broadening and shifting of the centroid of the Bragg peak has been reported in previous studies.[41,42]

The observed asymmetries in the diffraction pattern imply that the (110) atomic planes and another set of tilted planes within the nanocrystal satisfy the same Bragg condition. The fringe

oscillations and striped nature within one split peak correspond to the population of individual domains of a certain orientation along the given (110) atomic planes. We utilize phase retrieval algorithms (see experimental) to reconstruct the complex 3D Bragg electron density from the measured (110) Bragg peak with 18 nm spatial resolution as determined by the phase retrieval transfer function. The amplitude of the reconstructed complex Bragg electron density corresponds to the shape of the nanocrystal as shown in Figure 1, while the reconstructed phase encodes the atomic displacement fields of the (110) planes. A maximum intensity projection of the reconstructed amplitude of our BTO nanocrystal is depicted in Figure 1. The surface regions of the nanocrystal have a relatively uniform distribution of the amplitudes corresponding to uniform physical density of the crystal at its surface. However, the core of the nanocrystal has a distinct periodic "stripe-like" phase corresponding to a stripe variation of the physical density. In **Figure 2** we observe that the stripe phase is present in both the amplitude and displacement along two projections of the nanocrystal depicted as the "YX" and "ZX" planes respectively. The third plane (namely the "YZ" plane) is stripe-less and serves as a mirror plane to the stripe phases.

The reconstructed displacement field for the (110) atomic planes also depicts a characteristic stripe-like phase along the "YX" and "ZX" planes respectively as shown in Figure 2(B). From the experimentally reconstructed displacement field distribution $\mathbf{u}_{110}(\boldsymbol{r})$, we estimated the total elastic displacement gradients and strain ϵ_{ij} using the relationship $\epsilon_{ij} = 1/2\ (\partial \mathbf{u}^{i}_{110} / \partial x_j + \partial \mathbf{u}^{j}_{110} / \partial x_i)$. The spontaneous elastic strain in terms of the ferroelectric polarization is given by Equation (1)

$$\epsilon^{o}_{ij} = Q_{ijkl} P_k P_l \qquad (1)$$

where Q_{ijkl} is the electrostrictive tensor, ϵ^{o}_{ij} is the spontaneous strain, and the projections of the ferroelectric polarization along the *x*, *y* and *z* directions are given by P_k and P_l. The 3D displacement field in Figure 2(B) is indicative of a ferroelastic stripe phase with "needle-like"

polytwinned domains in the nanoparticle. These polytwinned structures mediate the modification of the crystal structure through long range ferroelastic order. In order to accommodate the structural inhomogeneity, BTO materials tend to develop mesostructures (strain inhomogeneity, twin domains, etc.) within the volume of the BTO nanocrystal (Figure 2 and **Figure 3**).

In phase retrieval, a maximum phase shift in the complex density of 3.14 radians will correspond to a total displacement (relative to the ideal crystal lattice) of about $d_{hkl}/2$ for a given {hkl} atomic spacing. Such a displacement (associated with maximum phase shift) will correspond to symmetry breaking periodic ferroelectric stripe oscillations. However, in our retrieved displacement field distribution (see Figure 2) for the {110} atomic spacings, the maximum displacement varies from - $d_{110}/4$ to +$d_{110}/4$. We interpret this to indicate the presence of elastic domains rather than electric domains. The patterns near the surface of the particle differ from those within the volume, consistent with assertions made in previous works.[39,43]

We estimated the electrostrictive coefficients as a fitting parameter with the aid of Equation 1. The elastic coefficients used in the fit are consistent with phase field simulations (see Supplementary Note 1 and Supplementary Table 1). Since the displacements $\mathbf{u}_{110}(r)$ are relatively small compared to the size of the nanocrystal, the assumption that $\mathbf{u}_{110}(r)$ scales with the local polarization is justified by a summation of Born effective charges.[5,44,45] Figure 3 compares the experimental displacement gradients with Landau theoretical phase-field model predictions, and shows that the phase-field simulated distribution of the 3D elastic domains and ferroelectric polarization distribution in the nanocrystal agrees with observations.

The atomic structure at the domain boundary is not, in general, the same as in the bulk of the nanocrystal, due to differences in the forces acting on atoms. The size effect often plays an important role on the domain structures of ferroelectric thin films and nanoparticles. It has been shown that for ferroelectric thin films, the domain size scales as the square root of the crystal thickness.[46,47] In ferroelectric nanoparticles, the relationship between the domain size w and the particle size is estimated by:[48]

$$w^2 = \frac{\sqrt{2}}{2}\frac{\sigma}{\frac{U_x}{x}+\frac{U_y}{y}+\frac{U_z}{z}} \quad (2)$$

where σ is a constant, and U_x, U_y, U_z are constants proportional to the surface energy density. The coordinates x, y, and z represent the length scales along the three axes. This indicates that smaller nanoparticles prefer smaller domain sizes. Thus, the needle-like domains seen at the nanoscale are induced by the small size of the particle. From Figure 1 and Figure 2, we conclude that our BTO nanocrystal has an intermediate mesostructural length scale, with stripe phases in two global planes of the nanoparticle YX and ZX and locally within these individual planes. Our displacement field reconstructions in Figure 2 show that elastic domain features (size, sources, sinks) behave differently for regions of the nanocrystal that have compressive and tensile strain. We are interested in: (i) the local structure and evolution of the domains under axial tensile and compressive stresses, (ii) the net ferroelectric polarization evolution as a function of axial stress, and (iii) mechanical switching of the domains. Similarly, how does the structure-property interplay influence structural phase transitions within individual nanocrystals?

To investigate these relationships, we utilize Landau theory to interpret the experimentally observed 3D elastic domain structure. **Figure S1** shows 3D domain orientation, and a central slice of the domain structure and polarization distribution for the simulated particle in the unperturbed state. The tetragonal phase [100] and [010] (oriented) domains are separated by

90°elastic domain walls, in agreement with the diffraction pattern of Figure 2. The twinned elastic domains are sensitive to an external field. **Figure 4**(A) shows the evolution of the domain morphology under uniaxial stress. Under a positive axial stress S_{11} along the x axis, the size of [100] domains increase whereas the [010] domains are suppressed. The number of twinned domains decreases as S_{11} increases from 0 to 0.13 GPa to 0.27 GPa. However, when S_{11} is negative (i.e. S_{11} is a compressive stress), the [100] domain is suppressed, and the domain structure transforms to pure {001}/{010} twinned domains at S_{11}=-0.27 GPa. Figure 4(B) shows the polarization components P_x, P_y, P_z versus the applied stress field S_{11}. At S_{11}=-0.27 GPa, P_x is almost zero indicating {010}/{001} twinned domains. With increasing S_{11}, P_x increases whereas P_y and P_z decrease. At S_{11}=0.27 GPa, P_z decreases to zero. This result indicates that the twinned structure undergoes a transformation from {010}/{001} twins to {100}/{010} twins with increasing axial stress S_{11}. The phase structure remains tetragonal as S_{11} changes. However, with applied principal stresses (i.e. S_{11}=S_{22}=S_{33}=S_0) along three axial directions, a transformation in the domain structure can be induced. As show in **Figure 5**(A), as S_0 changes from -0.6 to 1.2 GPa, the phase structures transform from pure tetragonal phase to tetragonal-orthorhombic phases to orthorhombic-rhombohedral phases. Figure 5(B) shows the magnitude of the maximum polarization vs. the axial stress S_0 in the nanoparticle. The maximum polarization decreases as S_0 decreases and there is a critical value of S_0 at -0.7 GPa, below which the phase transforms from ferroelectric to paraelectric. Figure 5(B, inset) shows the polarization vs. stress loop at small signal field, showing that the needle-like twin domains are reversible at small signal stress field S_{11} below 0.1 GPa.

3. Conclusion

We have demonstrated the ability to image ferroelastic domains in ferroic BTO which opens avenues for studying ferroelastic domain wall evolution under external stress and electric field *in operando*. This builds off existing studies of macroscopic and surface characterizations of ferroelastic materials as the morphology of the ferroelastic domains is directly imaged rather than inferred. Using BCDI we have captured the needle-like twinned structures in a 3D BTO nanoparticle. The domain morphology seen is consistent with the results of our Landau

simulations using clamped boundary conditions which force the displacements at the surface to be zero. The polarization outside the surface is assumed to be zero as the matrix is essentially amorphous. As the size of the particle increases, the needle like domains are lost in the simulations, emphasizing the importance of the surface. The needle twinned domains are mobile, structural, and a transformation can be induced with applied axial stress field. At low stress field, we show a mechanical hysteresis of the needle-like twin domains. With axial field S_{11}, the phase remains tetragonal. However, there is a transformation from {010}/{001} twins to {100}/{010} twins. The principal stress S_0 is applied along three axial directions. For S_0 below -0.7 GPa, the compressive stress leads to a ferroelectric-to-paraelectric transformation. With S_0 increasing from 0 to 1.2 GPa, the domain structure transforms to a T-O and O-R phase mixture.

Experimentally, our observations so far have not been for varying nanoparticle sizes or in the presence of fields such as stress to observe the phase transformations and evolution of domain and boundaries that Landau theory predicts. However, future experimental modifications to BCDI (e.g. flexible sample environments) will clearly need to be designed to verify the predictions of the simulations. Our observation of a diffuse cloud about the measured X-ray Bragg peak might suggest the possibility of a tweed structural pattern in our sample. With increasing interest in functionalizing ferroelastic boundaries, especially in multiferroics, our work, with its focus on new experimental tools related to coherent diffraction imaging, provides unique opportunities for testing standing models and understanding complex pattern formation.

4. Experimental Section

Experiment: BTO nanocrystals were synthesized via the sol-gel-hydrothermal reaction of $BaCl_2$ and a $TiCl_4$ solution in oxygen atmosphere. X-ray powder diffraction was used to confirm the crystalline nature of the BTO nanocrystals. By later performing scanning electron microscopy (Figure S1a) we observed that the BTO nanocrystals were formed with well-defined shapes and random orientations. The random orientation of the nanocrystals allowed us to isolate the (110) Bragg coherent diffraction peak from an individual BTO nanocrystal in our experiment.[49] To record the 3D diffraction data (see Figure 1), we rocked the sample with respect to the incident X-ray beam.

A Si (111) monochromator at sector 34-ID-C of Advanced Photon Source was used to select coherent X-ray photons with an energy of 9.0 keV. The monochromaticity of the beam given by the energy bandwidth was 1eV. This allows us to prescribe and utilize a transverse beam coherence length of 0.7 μm. A monochromatic, coherent, x-ray beam focused by Kirkpatrick-

Baez mirrors (not shown in Figure 1) was used to create a localized illumination spot of about 700 nm by 700 nm on the sample. A motorized arm was used to position the location of a Medipix2 CMOS X-ray detector (with pixel size of 55µm X 55µm) around the diffraction sphere. The detector position was aligned with the outgoing (110) characteristic Bragg reflection from the BTO sample. We positioned the detector at a distance of 0.65m from the sample to zoom into the interference fringes in the (110) diffraction pattern.

The rocking curve was collected by rotating the crystal about the Bragg condition in small increments of about 0.004^{o}. This allowed us to collect a series of 2D diffraction patterns in the vicinity of the BTO (110) Bragg peak corresponding to $2\theta = 28.196°$ with the scanning range of $\Delta\theta = \pm 0.20°$ about the Bragg peak origin. Throughout a single rocking curve, a total scan of 100 patterns was collected.

Phase Retrieval and Reconstruction procedure: Iterative phase retrieval algorithms were used to invert the diffraction data into 3D real space images that confirm a model predicted by Landau theory. We utilized iterative phase retrieval algorithms based on Fienup's hybrid input-output method combined with randomized over-relaxation.[50] Inverting the diffraction data is a critical step that uses a computer algorithm that takes advantage of internal redundancies when the measurement points are spaced close enough together to meet the oversampling requirement.[51]

We first postulate a 3D support volume. The entire sample density is constrained to exist within this support. We utilize an inverse and forward Fourier transform to iterate between reciprocal and real-space, with the support constraint imposed in the latter and an intensity mask constraint in the former.[42] The recorded 3D diffraction pattern (see Figure 1) in reciprocal space is then inverted into a direct space 3D image of the nanoparticle after the phase Φ and amplitude Q of the complex wave-field $\rho(r) = Q(r)e^{i\Phi(r)}$ are iteratively retrieved.[5]

The reconstructed phases Φ scale linearly with the displacement field $\mathbf{u}_{110}$ for a given reciprocal lattice vector $\mathbf{G}_{110}$ according to the relationship $\Phi(\mathbf{r})=\mathbf{G}_{110}\cdot\mathbf{u}_{110}$. The shape and size of the nanoparticle can be estimated from an isosurface of the reconstructed Bragg electron density (see Figure 1) given as the amplitude. The 3D real-space images (Figure 1, Figure2) of the individual $BaTiO_3$ nanoparticles shown in manuscript were reconstructed with approximately 18 nm spatial resolution as determined by a phase retrieval transfer function.[5] The reconstruction allows us to conveniently slice through the volume of the nanoparticle and analyze signatures of the ferroelastic domains along any given cartesian projection (Figure 2). From the retrieved displacement field $\mathbf{u}_{110}$, we are able to mathematically extract the spatial gradients of the displacement field (representing strain components) as shown in Figure 3.

Simulation: In the phase field simulation, the temporal evolution of the domain structure can be obtained by solving the time dependent Landau-Ginsburg equation:[52–56]

$$\frac{\partial P_i(\mathbf{r})}{\partial t} = -L\frac{\delta F}{\delta P_i(\mathbf{r})}, \quad i = 1,2,3$$

where L is the kinetic coefficient and $P_i(\mathbf{r})$ is the polarization component. F denotes the total free energy of the ferroelectric system, which is written as: $F = F_p + F_{el} + F_c + F_g$, where F_p is the Landau free energy, F_{el} is the elastic free energy, F_c is the electrostrictive free energy, and F_g is the gradient energy. The surface energy due to the depolarization is integrated into the electric static energy F_e. The details are given in Ref. [55]. A 56×64×64 grid mesh with periodic boundary condition has been used for the simulations of the nanoparticle embedded in the polymer matrix. Clamped boundary conditions are used for the calculation of the elastic displacements. The shape data of the nanoparticle is obtained from experiment and the amorphous region on the outside of the nanoparticle has its polarization set to zero. The Landau parameters for $BaTiO_3$ are taken from Ref. [57] and given in **Table S1**. The relative background permittivity ε_b is set to 2000.

Supporting Information
Supporting Information is available from the Wiley Online Library or from the author.

Acknowledgements
Raw data was measured at the Advanced Photon Source Sector 34-ID-C and are permanently deposited there. The data supporting the findings of this study are available from the corresponding author upon request.
This work was supported by the Air Force Office of Scientific Research under Award No. FA9550-14-1-0363 (Program Manager: Dr. Ali Sayir) and by Laboratory Directed Research and Development program at Los Alamos National Laboratory (LANL). We also acknowledge support in part from the LANSCE Professorship sponsored by the National Security Education Center at LANL under subcontract No. 257827. This research used resources of the Advanced Photon Source (APS), a U.S. Department of Energy (DOE) Office of Science User Facility operated for the DOE Office of Science by Argonne National Laboratory (ANL) under contract no. DE-AC02-06CH11357. We thank the staff at ANL and the APS for their support.
E.F. designed and conceived the project. E.F., D.K., E.S, and R.H performed the BCDI measurements and E.F. performed the phase retrieval analysis. Z.L. and T.L. performed the theoretical Landau phase field computation and theoretical interpretation. E.F. wrote the manuscript with contributions from all authors.

Received: ((will be filled in by the editorial staff))
Revised: ((will be filled in by the editorial staff))
Published online: ((will be filled in by the editorial staff))

References

[1] M. Dawber, K. M. Rabe, J. F. Scott, *Rev. Mod. Phys.* **2005**, *77*, 1083.
[2] N. Setter, D. Damjanovic, L. Eng, G. Fox, S. Gevorgian, S. Hong, A. Kingon, H. Kohlstedt, N. Y. Park, G. B. Stephenson, I. Stolitchnov, A. K. Taganstev, D. V. Taylor, T. Yamada, S. Streiffer, *J. Appl. Phys.* **2006**, *100*, 051606.
[3] O. Auciello, J. F. Scott, R. Ramesh, *Phys. Today* **1998**, *51*, 22.
[4] J. F. Scott, *Science (80-.).* **2007**, *315*, 954.
[5] D. Karpov, Z. Liu, T. D. S. Rolo, R. Harder, P. V. Balachandran, D. Xue, T. Lookman, E. Fohtung, *Nat. Commun.* **2017**, *8*, 280.
[6] V. Nagarajan, A. Roytburd, A. Stanishevsky, S. Prasertchoung, T. Zhao, L. Chen, J. Melngailis, O. Auciello, R. Ramesh, *Nat. Mater.* **2003**, *2*, 43.
[7] E. A. Little, *Phys. Rev.* **1955**, *98*, 978.
[8] R. Xu, S. Liu, I. Grinberg, J. Karthik, A. R. Damodaran, A. M. Rappe, L. W. Martin, *Nat. Mater.* **2015**, *14*, 79.
[9] J. Hoffman, X. Pan, J. W. Reiner, F. J. Walker, J. P. Han, C. H. Ahn, T. P. Ma, *Adv. Mater.* **2010**, *22*, 2957.
[10] R. Xu, J. Karthik, A. R. Damodaran, L. W. Martin, *Nat. Commun.* **2014**, *5*, 3120.
[11] S. V. Kalinin, B. J. Rodriguez, A. Y. Borisevich, A. P. Baddorf, N. Balke, H. J. Chang, L.-Q. Chen, S. Choudhury, S. Jesse, P. Maksymovych, M. P. Nikiforov, S. J. Pennycook, *Adv. Mater.* **2010**, *22*, 314.
[12] C. T. Nelson, P. Gao, J. R. Jokisaari, C. Heikes, C. Adamo, A. Melville, S.-H. Baek, C. M. Folkman, B. Winchester, Y. Gu, Y. Liu, K. Zhang, E. Wang, J. Li, L.-Q. Chen, C.-B. Eom, D. G. Schlom, X. Pan, *Science* **2011**, *334*, 968.

[13] Á. Butykai, S. Bordács, I. Kézsmárki, V. Tsurkan, A. Loidl, J. Döring, E. Neuber, P. Milde, S. C. Kehr, L. M. Eng, *Sci. Rep.* **2017**, *7*, 44663.
[14] E. K. H. Salje, *Annu. Rev. Mater. Res.* **2012** *42*, 265.
[15] G. Arlt, *J. Mater. Sci.* **1990**, *25*, 2655.
[16] G. Catalan, J. Seidel, R. Ramesh, J. F. Scott, *Rev. Mod. Phys.* **2012**, *84*, 119.
[17] D. Meier, *J. Phys. Condens. Matter* **2015**, *27*, 463003.
[18] D. Meier, J. Seidel, A. Cano, K. Delaney, Y. Kumagai, M. Mostovoy, N. A. Spaldin, R. Ramesh, M. Fiebig, *Nat. Mater.* **2012**, *11*, 284.
[19] M. Schröder, X. Chen, A. Haußmann, A. Thiessen, J. Poppe, D. A. Bonnell, L. M. Eng, *Mater. Res. Express* **2014**, *1*, 035012.
[20] F. Kagawa, M. Mochizuki, Y. Onose, H. Murakawa, Y. Kaneko, N. Furukawa, Y. Tokura, *Phys. Rev. Lett.* **2009**, *102*, 057604.
[21] J. Seidel, L. W. Martin, Q. He, Q. Zhan, Y. H. Chu, A. Rother, M. E. Hawkridge, P. Maksymovych, P. Yu, M. Gajek, N. Balke, S. V. Kalinin, S. Gemming, F. Wang, G. Catalan, J. F. Scott, N. A. Spaldin, J. Orenstein, R. Ramesh, *Nat. Mater.* **2009**, *8*, 229.
[22] A. Aird, E. K. H. Salje, *J. Phys. Condens. Matter* **1998**, *10*, L377.
[23] E. A. Eliseev, A. N. Morozovska, Y. Gu, A. Y. Borisevich, L. Q. Chen, V. Gopalan, S. V. Kalinin, *Phys. Rev. B - Condens. Matter Mater. Phys.* **2012**, *86*, 085416.
[24] P. Gao, J. Britson, C. T. Nelson, J. R. Jokisaari, C. Duan, M. Trassin, S.-H. Baek, H. Guo, L. Li, Y. Wang, Y.-H. Chu, A. M. Minor, C.-B. Eom, R. Ramesh, L.-Q. Chen, X. Pan, *Nat. Commun.* **2014**, *5*, 3801.
[25] E. K. H. Salje, S. A. Hayward, W. T. Lee, *Acta Crystallogr. Sect. A Found. Crystallogr.* **2005**, *61*, 3.
[26] Y. Ivry, N. Wang, D. Chu, C. Durkan, *Phys. Rev. B* **2010**, *81*, 174118.
[27] G. Arlt, P. Sasko, *J. Appl. Phys.* **1980**, *51*, 4956.
[28] C.-L. Jia, S.-B. Mi, K. Urban, I. Vrejoiu, M. Alexe, D. Hesse, *Nat. Mater.* **2008**, *7*, 57.
[29] F. Jona, G. Shirane, *Ferroelectric Crystals*, Dover publications, Mineola, NY, **1993**.
[30] M.-G. Han, Y. Zhu, L. Wu, T. Aoki, V. Volkov, X. Wang, S. C. Chae, Y. S. Oh, S.-W. Cheong, *Adv. Mater.* **2013**, *25*, 2415.
[31] M. J. G. Cottet, M. Cantoni, B. Mansart, D. T. L. Alexander, C. Hébert, N. D. Zhigadlo, J. Karpinski, F. Carbone, *Phys. Rev. B* **2013**, *88*, 014505.
[32] J. Chen, G. Conache, M.-E. Pistol, S. M. Gray, M. T. Borgström, H. Xu, H. Q. Xu, L. Samuelson, U. Håkanson, *Nano Lett.* **2010**, *10*, 1280.
[33] I. Robinson, R. Harder, *Nat. Mater.* **2009**, *8*, 291.
[34] E. Fohtung, J. W. Kim, K. T. Chan, R. Harder, E. E. Fullerton, O. G. Shpyrko, *Appl. Phys. Lett.* **2012**, *101*, 033107.
[35] G. H. Kwei, A. C. Lawson, S. J. L. Billinge, S. W. Cheong, *J. Phys. Chem.* **1993**, *97*, 2368.
[36] S. J. Leake, V. Favre-Nicolin, E. Zatterin, M. I. Richard, S. Fernandez, G. Chahine, T. Zhou, P. Boesecke, H. Djazouli, T. U. Schülli, *Mater. Des.* **2017**, *119*, 470.
[37] S. A. Hayward, E. K. H. Salje, *Zeitschrift fur Krist.* **2005**, *220*, 994.
[38] J. Chrosch, E. K. H. Salje, *Ferroelectrics* **1997**, *194*, 149.
[39] C. Mathieu, C. Lubin, G. Le Doueff, M. Cattelan, P. Gemeiner, B. Dkhil, E. K. H. Salje, N. Barrett, *Sci. Rep.* **2018**, *8*, 13660.
[40] O. Aktas, M. A. Carpenter, E. K. H. Salje, *Appl. Phys. Lett.* **2013**, *103*, 142902.
[41] A. A. Minkevich, E. Fohtung, T. Slobodskyy, M. Riotte, D. Grigoriev, T. Metzger, A. C. Irvine, V. Noávk, V. Holk, T. Baumbach, *Epl* **2011**, *94*.
[42] A. A. Minkevich, E. Fohtung, T. Slobodskyy, M. Riotte, D. Grigoriev, M. Schmidbauer, A. C. Irvine, V. Novák, V. Holý, T. Baumbach, *Phys. Rev. B* **2011**, *84*, 054113.
[43] N. Barrett, J. Dionot, D. Martinotti, E. K. H. Salje, C. Mathieu, *Appl. Phys. Lett.* **2018**,

113, 022901.
[44] D. D. Fong, C. Cionca, Y. Yacoby, G. B. Stephenson, J. A. Eastman, P. H. Fuoss, S. K. Streiffer, C. Thompson, R. Clarke, R. Pindak, E. A. Stern, *Phys. Rev. B* **2005**, *71*, 144112.
[45] G. Sághi-Szabó, R. E. Cohen, H. Krakauer, *Phys. Rev. Lett.* **1998**, *80*, 4321.
[46] A. Schilling, T. B. Adams, R. M. Bowman, J. M. Gregg, G. Catalan, J. F. Scott, *Phys. Rev. B* **2006**, *74*, 024115.
[47] J. F. Scott, *J. Phys. Condens. Matter* **2006**, *18*, R361.
[48] G. Catalan, A. Schilling, J. F. Scott, J. M. Gregg, *J. Phys. Condens. Matter* **2007**, *19*, 132201.
[49] B. Abbey, *JOM* **2013**, *65*, 1183.
[50] M. Köhl, A. A. Minkevich, T. Baumbach, *Opt. Express* **2012**, *20*, 17093.
[51] D. Sayre, *Acta Crystallogr.* **1952**, *5*, 843.
[52] S. Nambu, D. A. Sagala, *Phys. Rev. B* **1994**, *50*, 5838.
[53] L.-Q. Chen, *J. Am. Ceram. Soc.* **2008**, *91*, 1835.
[54] Z. Liu, B. Yang, W. Cao, T. Lookman, *Phys. Rev. B* **2016**, *94*, 214117.
[55] Z. Liu, B. Yang, W. Cao, E. Fohtung, T. Lookman, *Phys. Rev. Appl.* **2017**, *8*, 034014.
[56] H.-L. Hu, L.-Q. Chen, Three-Dimensional Computer Simulation of Ferroelectric Domain Formation. *J. Am. Ceram. Soc.* **2005**, *81*, 492.
[57] T. Sluka, A. K. Tagantsev, D. Damjanovic, M. Gureev, N. Setter, *Nat. Commun.* **2012**, *3*, 748.

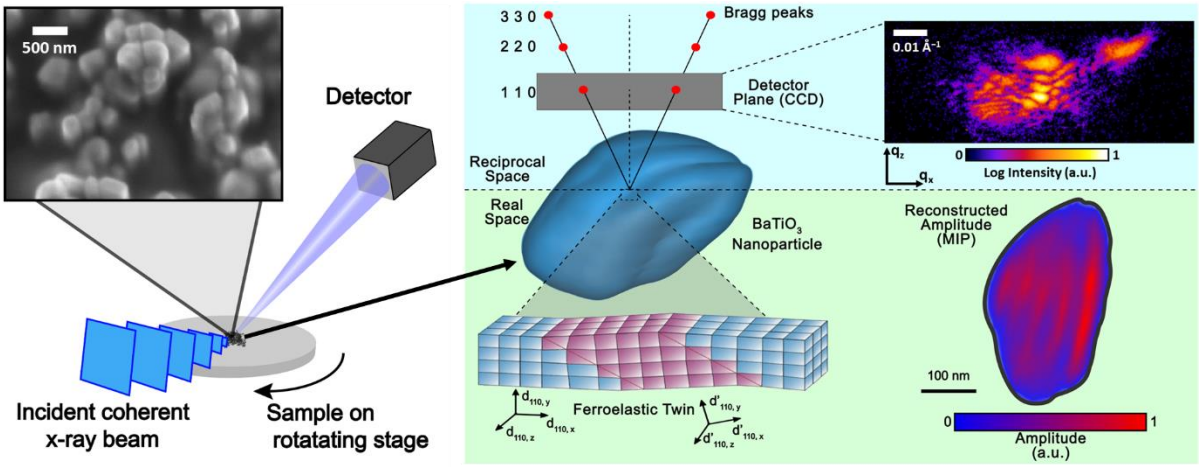

Figure 1. Schematic of typical BCDI experiment and BCDI reconstructed BTO nanoparticle shape with a schematic illustrating the origin of our measured split diffraction peak. A maximum intensity projection (MIP) of the reconstructed amplitude is inset, showing fluctuations indicative of a variation of Bragg plane populations.

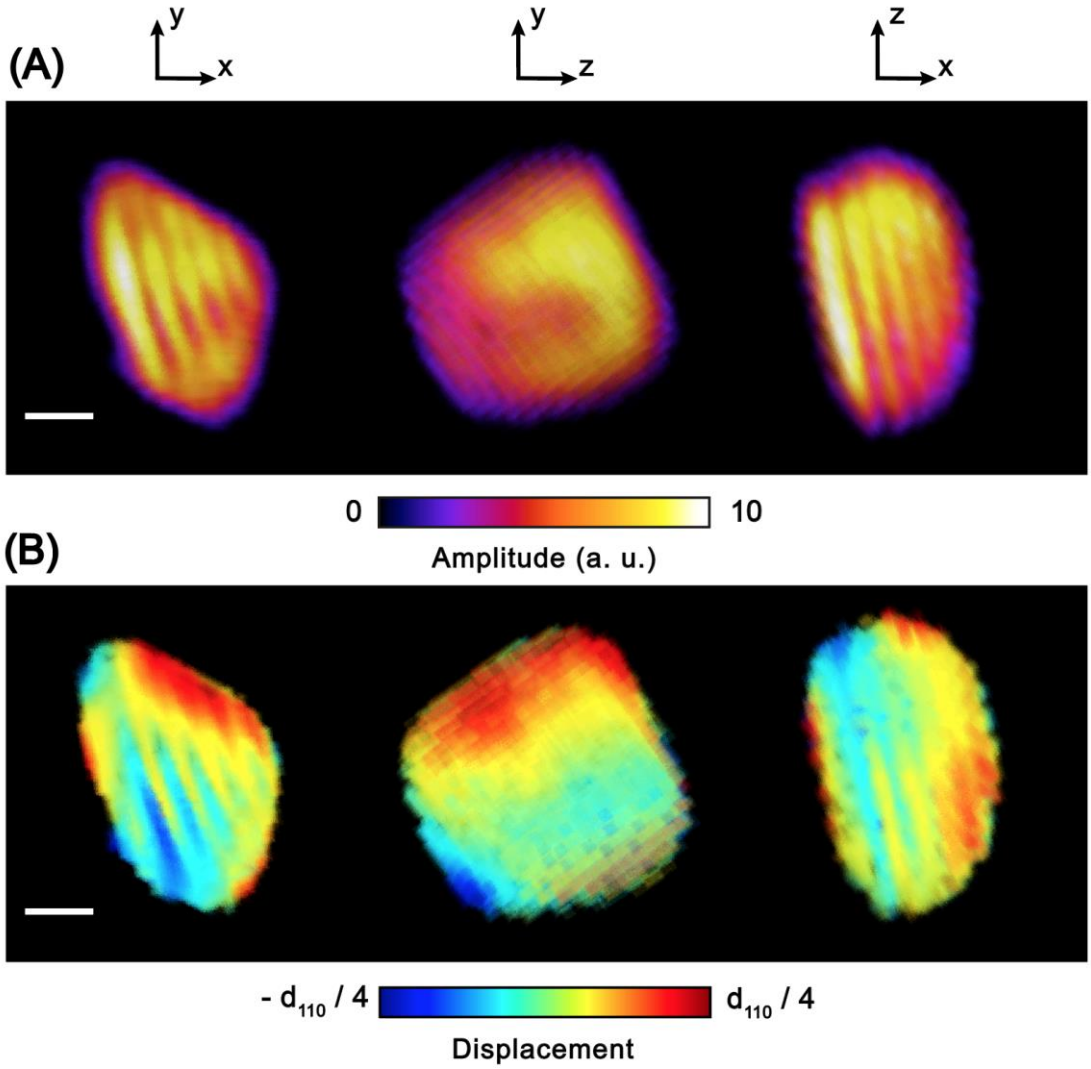

Figure 2. Volumetric BCDI reconstructions of **(A)** the amplitude and (**B**) the displacements of the complex Bragg electron density from the 110 Bragg peak. Scale bars correspond to 100 nm.

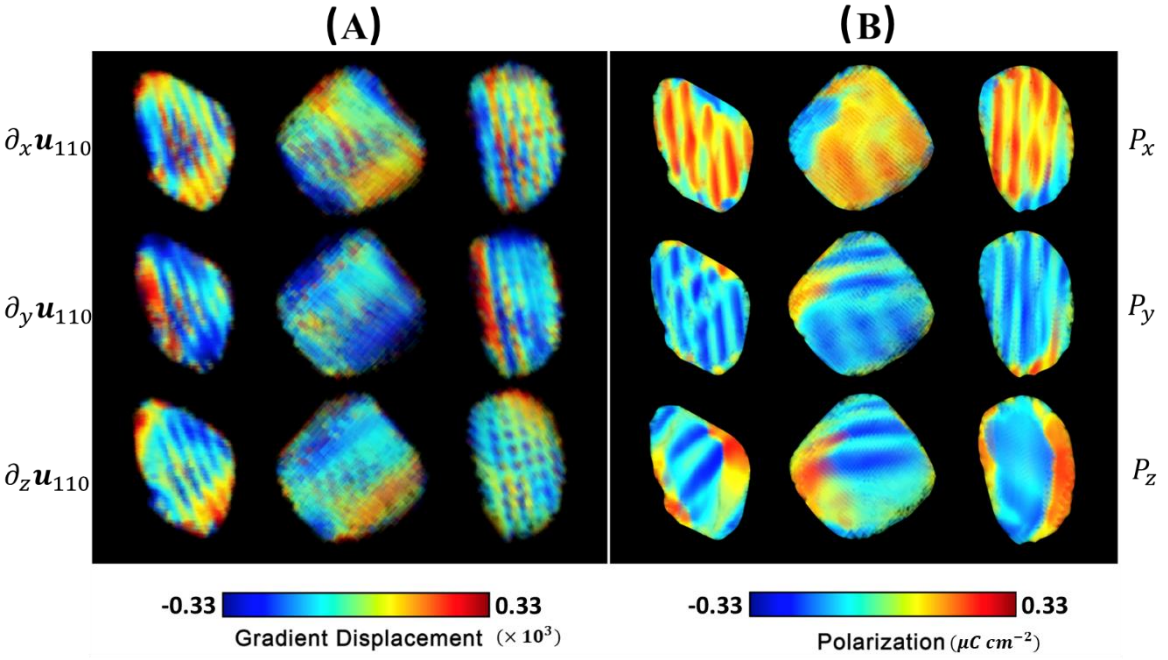

Figure 3. (A) Experimentally reconstructed components of the elastic strain tensor (component). Slices through the nanocrystal volume at three orthogonal slice planes halfway through the particle showing the inhomogeneity of the elastic strain mediating the presence of needle domains. **(B)** Phase-field simulations of polarization for similar cut planes.

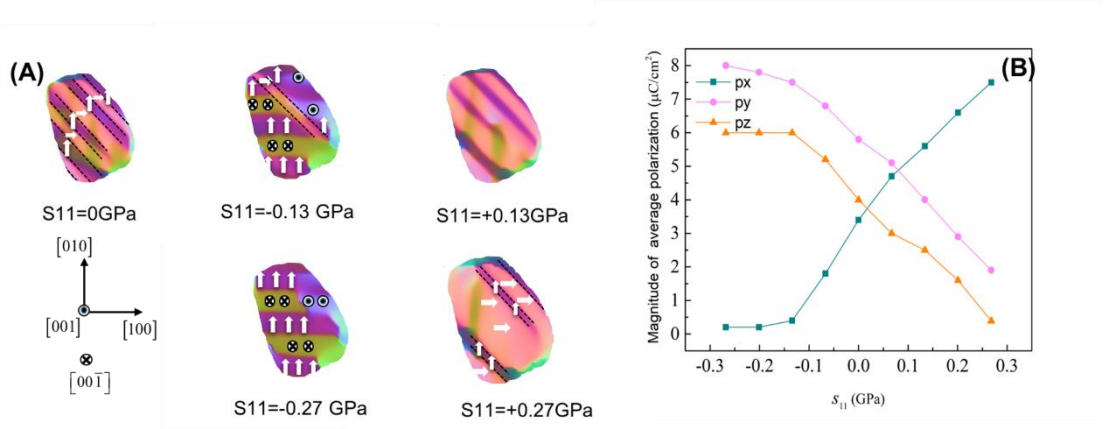

Figure 4. (A) Domain orientation vs. applied axial stress S_{11} predicted by Landau calculations. **(B)** Magnitude of polarization components vs. applied axial stress S_{11}.

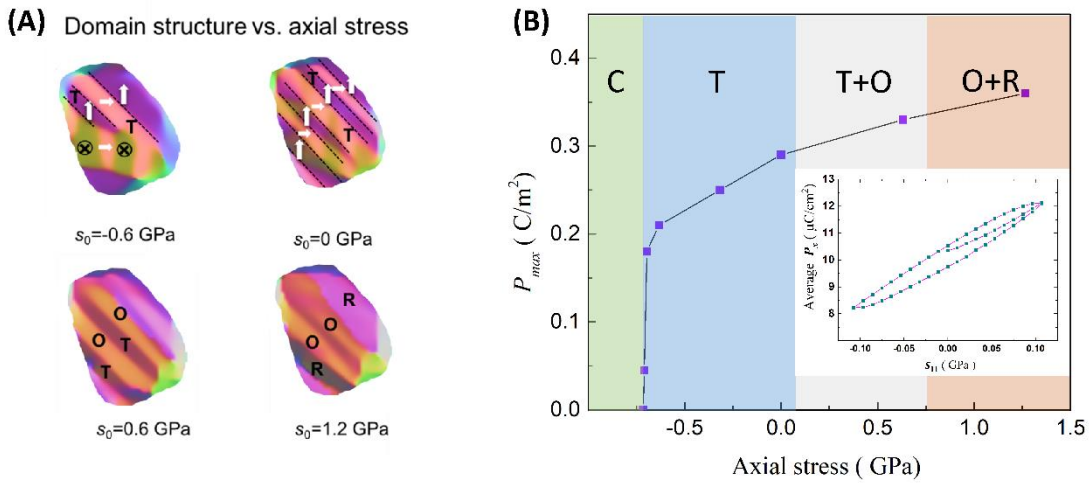

Figure 5. (A) Landau phase-field simulations of the 3D domain morphology under applied stress. **(B)** Phase diagram showing maximum polarization vs applied axial stress **Inset:** Average polarization vs applied stress showing hysteresis at small stress field

Table of Contents Entry:
Ferroelastic domains within the volume of a ferroelectric nanoparticle are imaged using coherent X-rays and phase retrieval. Using a Landau theoretical simulation, domain boundaries are shown to be highly labile under applied stress, and induce polarization and structural/ferroelectric phase transitions within the particle. This study makes the anticipated functionalization of ferroelastic boundaries one step closer to realization.

Ferroelasticity *((choose a broad keyword related to the research))*

*Z. Liu, E. Schold, D. Karpov, R. Harder, T. Lookman, and E. Fohtung**

Needle-like Ferroelastic Domains in Individual Ferroelectric Nanoparticles

ToC figure

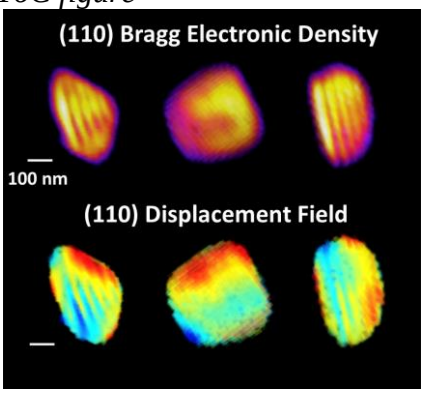

Supporting Information

Needle-like Ferroelastic Domains in Individual Ferroelectric Nanoparticles

*Zhen Liu, Elijah Schold, Dmitry Karpov, Ross Harder, Turab Lookman, and Edwin Fohtung**

Supplementary Table 1: Elastic and Electrostrictive coefficients used for Landau simulation of ferroelastic particle

C_{11} [10^{11}N m^{-2}]	C_{12} [10^{11}N m^{-2}]	C_{44} [10^{11}N m^{-2}]	Q_{11} [C^{-2} m^4]	Q_{12} [C^{-2} m^4]	Q_{44} [C^{-2} m^4]
1.78	0.964	1.22	0.10,0.11	-0.034, 0.045	0.029, 0.059

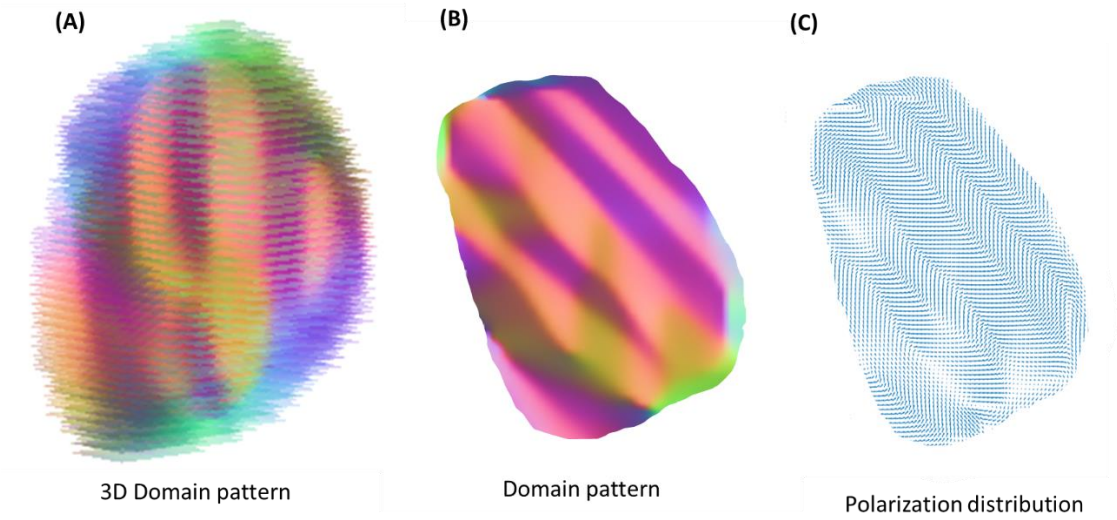

Supplementary Figure 1. (A) Landau phase-field simulation of the 3D domain. **(B)** 2D central slice of the domain pattern and **(C)** the ferroelectric polarization distribution